JOURNAL OF MATERIALS SCIENCE **36** (2001) 2179–2188

A comparative discrete-dislocation/ crystal-plasticity analysis of bending of a single-crystalline microbeam

M. GRUJICIC, D. COLUMBUS
Department of Mechanical Engineering, Clemson University, Clemson, SC 29634-0921, USA
E-mail: mica@ces.clemson.edu

Bending of a micron-size single-crystalline beam is analyzed using both discrete-dislocation plasticity and crystal-plasticity formulations. Within the discrete-dislocation plasticity formulation, dislocations are treated as infinitely long straight-line defects residing within a linear elastic continuum. Evolution of the dislocation structure during bending is simulated by allowing the dislocations to glide in response to long-range interactions between different dislocations, and between dislocations and the applied stresses, and by incorporating various short-range reactions which can result in dislocation nucleation, annihilation or pinning. At each stage of bending, the stress and deformation fields are obtained by superposing the dislocation fields and the complementary fields obtained as a solution of the corresponding linear-elastic boundary value problem. The results obtained show that there is a continuing accumulation of "geometrically necessary" dislocations during bending which is expected due to the gradient in the strain throughout the beam height. In addition, it is found that localization of plastic flow into slip bands is a salient feature of materials deformation at the micron-length scale. Within the crystal-plasticity analysis, of beam bending, a small displacement gradient formulation is used and the material parameters selected in such a way that plastic flow localizes into deformation bands at low strains. It is found that, while the global response of the beam predicted by the two approaches can be quite comparable, fine details of the dislocation-based stress and deformation fields cannot be reproduced by the continuum crystal-plasticity model.

1. Introduction

The behavior of isotropic linear elastic and isotropic elastic-plastic beams subjected to pure bending is relatively simple and well established. In linear elastic beams, the normal stress parallel to the bending axis is distributed linearly in the through-the-height direction, with the inner and outer layers of the beam subjected to the maximum stresses of the opposite sign. Under the condition of equal yield stress of the material under the uniaxial tension and compression conditions, the onset of plastic yielding in an elastic-plastic beam, takes place simultaneously at the outer and inner surfaces of the beam. As bending continues, the plastic zone advances toward the centerline of the beam. For an ideal plastic material, the plastic zone reaches the centerline at a critical value of the bending moment, which is equal to 1.5 times its value at the onset of plastic yielding. Due to inability of the beam to support any additional bending load, plastic buckling occurs. Similar buckling does not take place in beams made of strain-hardening materials. In contrast to the isotropic beams, the behavior of anisotropic (e.g. single-crystalline) beams is more complex. During bending in the elastic region, the anisotropy of elastic properties substantially affects stress distribution throughout the beam. In the plastic region, plastic anisotropy arising from the crystallographic nature of the material and of deformation slip on a limited number of slip systems results in an even more pronounced dependence of the beam behavior on the orientation of the crystal lattice relative to the bending axis.

In recent years, a new field of design, analysis, and processes of micron-size structures and machines has emerged. Since many components in such microstructures and machines are subjected to in-service bending loads, understanding of the bending behavior of micron-size beams can provide the data needed in design of such micro-components. It should be noted that the micron-size components are generally composed of single crystalline materials. Hence, as discussed above, their behavior is intrinsically anisotropic and dependent on the orientation of the material's crystal structure. In addition, at the micron-length scale, the effect of discrete dislocations, in particular their long-range stress and deformation fields and short-range interactions which can result in dislocation nucleation and

annihilation and formation of pile-ups and patterns becomes important. Recently, Cleveringa *et al*. [1] carried out a detailed discrete-dislocation analysis of single-crystal beam bending which clearly showed the role of dislocations. In particular, it is found that dislocation nucleation and motion during bending are not purely stochastic but rather occur in such a way to produce the so-called "geometrically necessary" dislocations [2, 3]. The presence of such dislocations reduces the bending stresses within the beam considerably relative to the stresses predicted by the elastic continuum models. While the work of Cleveringa *et al*. [1] clearly demonstrated the important role discrete dislocations may play in affecting the material behavior at the micron-length scale, it also revealed that discrete-dislocation analysis is extremely computationally expensive. This may become a major hindrance for its use as a means of generating the materials property data at the micron-length scale. Namely, due to a stochastic nature of the discrete-dislocation approach, numerous simulation runs have to be made in order to obtain statistically reliable data needed in the desing of micron-size components.

In the present work, a comparative analysis of bending of a micron-size beam is carried out using discrete-dislocation plasticity and crystal-plasticity formulations. The main objective of the work is to establish if the crystal-plasticity approach, which is computationally quite less demanding, can reproduce the essential features of the materials deformation at the micron-length scale.

The organization of the paper is as follows: In Sections 2.1 and 2.2, the basic formulations of discrete-dislocation plasticity and crystal-plasticity are presented, respectively. The results obtained using both approaches are presented and discussed in Sections 3.1 and 3.2, respectively. Main conclusions resulting from the present work are summarized in Section 4.

2. Computational analysis

2.1. Discrete-dislocation formulation

Following Cleveringa *et al*. [1], a discrete dislocation analysis of bending of a single-crystalline beam is carried out using the formulation proposed by Van der Giessen and Needleman [4] and Cleveringa *et al*. [5]. Within this formulation, evolution of the deformation state and the dislocation structure during loading is computed in an incremental manner. At the beginning of a time increment at the t, the position of each dislocation in the body is known and the body is in equilibrium with the applied tractions and displacements. Then, for an increment in loading, the formulation of Van der Giessen and Needleman [4] and Cleveringa *et al*. [5] can be used to determine the equilibrium stress fields and the dislocation structure at the end of the time increment (time $= t + \Delta t$).

The main concept in the formulation proposed by Van der Giessen and Needleman [4] and Cleveringa *et al*. [5] is that the displacement, strain, and stress fields can be expressed as the superposition of two fields: (a) the ($\tilde{}$) fields which are, in turn, the result of superposition of the (infinite, homogeneous-medium) fields of individual dislocations in their current configuration. (Since the stress fields of individual dislocations are singular and hence not readily handled by numerical techniques such as the finite element methods, they are evaluated analytically.): and (b) the ($\hat{}$) complimentary fields associated with the imposed boundary conditions corrected for the effect of dislocations. Since the ($\hat{}$) fields are generally smooth, they can be determined by solving a conventional linear-elastic boundary-value problem using the finite element method.

Due to the intrinsic complexity of a three-dimensional analysis of the dislocation structure and its evolution, and the associated computational requirements, only a two-dimensional formulation is used. Within this formulation, dislocations are treated as infinitely long, straight, parallel and all of the edge character. They are allowed to interact with each other through their long-range stress fields and to affect the imposed traction and displacement boundary conditions. The infinite, homogeneous-medium dislocation stress and deformation fields which are used to compute the ($\tilde{}$) fields are readily available [e.g. 6, 7]. Only dislocation glide on well-defined slip planes is allowed and, hence, the change in the potential energy of the body due to a potential infinitesimal change in the position of the dislocation i results in the Peach-Koehler force f^i given by:

$$f^i = n^i \cdot \left(\hat{\sigma} + \sum_{j \neq i} \tilde{\sigma}^j \right) \cdot b^i \qquad (1)$$

where n^i is the corresponding slip plane normal, b^i the Burgers vector, and $\hat{\sigma}$ and $\tilde{\sigma}^i$ are the two stress fields discussed above. As indicated by Equation 1, the Peach-Koehler force includes the interactions of a given dislocation with the applied stress field and with all other dislocations in the material. The force is coplanar with the slip plane of the given dislocation and collinear with its Burgers vector. As a result of the Peach-Koehler force, each dislocation glides on its slip plane in the direction of the Peach-Koehler force. The magnitude of the glide velocity v^i of dislocation i is taken to be drag controlled, and hence, linearly related to the Peach-Koehler force as:

$$f^i = Bv^i \qquad (2)$$

where B is the drag coefficient. $B = 10^{-4}$ Pa·s is assumed in the present work which according to Kubin *et al*. [8] is a representative value for aluminum. When dislocation pile-ups are formed, the position of dislocations in them is quite unstable, leading to high-velocity oscillatory motions. To remove these essentially inconsequential effects, a cut-off velocity of 20 m/s is used. This value of the cut-off velocity is found to be low enough to eliminate the undesirable oscillations and yet high enough not to affect the results significantly.

In addition to the long-range dislocation interactions discussed above which contribute to the Peach-Koehler force and also affect the imposed boundary conditions, short-range dislocation-dislocation interactions which may result in nucleation and annihilation of dislocations are also considered. Dislocation nucleation is modeled by simulating the operation of Frank-Read sources.

Within the present two-dimensional formulation, point-type Frank-Read sources are considered which generate a dislocation dipole when the magnitude of the Peach-Koehler force at the source exceeds a critical value $\tau_{\text{nuc}}b$ (b is the magnitude of the Burgers vector which is set equal to 0.25 nm) during a time period t_{nuc}. The dipole separating distance L_{nuc} is taken to be dependent on the source strength τ_{nuc} as:

$$L_{\text{nuc}} = \frac{E}{4\pi(1-\nu^2)}\frac{b}{\tau_{\text{nuc}}} \tag{3}$$

where E and ν are the Young's modulus set to 70 GPa and the Poisson's ratio set to 0.33, respectively. At the distance L_{nuc}, the slip-plane resolved shear stress acting on one dislocation in the dipole due to its interaction with the other dislocation in the dipole is exactly balanced by the overall slip-plane resolved shear stress acting on the corresponding source. The strength of the dislocation sources, τ_{nuc}, is randomly chosen from a Gaussian distribution with mean strength $\bar{\tau}_{\text{nuc}} = 50$ MPa and standard deviation of $0.2\bar{\tau}_{\text{nuc}}$. Based on Equation (3), the mean nucleation distance is $L_{\text{nuc}} = 125.0b = 31.5$ nm. The nucleation time which mimics the time necessary for a stable dislocation loop to be generated at a Frank-Read source is set to a fixed value of $t_{\text{nuc}} = 0.01\ \mu$s for all sources. Following, Cleveringa *et al.* [1], a fixed time increment of $\Delta t = 5 \times 10^{-10}$ s is used in simulations. Consequently, timing of the individual events of dipole generation or annihilation may be slightly incorrect. Fortunately, these effects are found not to significantly affect the overall results.

Two dislocations with opposite Burgers vector gliding on the same slip plane are allowed to annihilate when they are with in a material-dependent, critical annihilation distance L_{e}. Following Cleveringa *et al.* [1], a fixed value $L_{\text{e}} = 6b = 1.5$ nm is used.

Since the material is taken to be of high purity, fixed, localized obstacles to dislocation motion (e.g. nano-precipitates, nano-inclusions) are not considered. Furthermore, short-range interactions between dislocations gliding on intersecting slip planes which can result in formation of various sessile dislocation configurations or locks of different strengths are not incorporated explicitly. Never the less, as will be shown later, when such dislocations are close to intersecting, their interactions through the stress fields can be so strong that they can render them essentially sessile.

The boundary value problem corresponding to plane-strain bending of a beam is shown schematically in Fig. 1. The beam has a width L, and height h, and its sides are subject to rotation. A (x_1, x_2) Cartesian coordinate system is used with its origin located at the beam midpoint and its axes parallel with the edges of the beam, Fig. 1. Thus the $x_1 - x_2$-plane is the plane of deformation and the boundary conditions for plane-strain beam bending can be defined as:

$$u_1 = \pm(\theta x_2 + U), \quad \sigma_{12} = 0 \quad \text{on} \quad x_1 = \pm L/2 \tag{4}$$

$$\sigma_{12} = 0, \quad \sigma_{22} = 0 \quad \text{on} \quad x_2 = \pm h/2 \tag{5}$$

where θ is the imposed angle of rotation on the left and the right sides of the beam. The work-conjugate

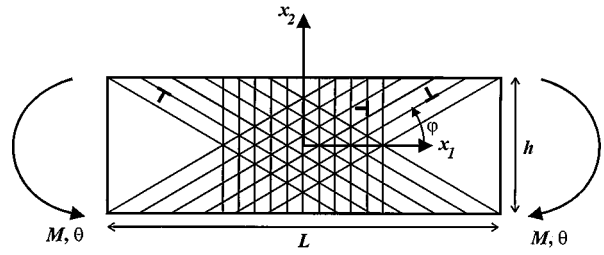

Figure 1 A schematic of the discrete-dislocation boundary value problem for plane-strain beam bending. Positive dislocations on each of the three slip systems are illustrated to indicate the sign convention used.

bending moment, M, is given by:

$$M = \int_{-h/2}^{h/2} x_2 \sigma_{11}(\pm L/2, x_2)\, dx_2 \tag{6}$$

During loading in the elastic regime, the only non-zero in-plane stress component is σ_{11} which varies linearly with x_2 between a maximum positive value at $x_2 = h/2$ and a maximum negative value at $x_2 = -h/2$. Also, the curvature k is uniform and equal to $2\theta/L$, while the quantity U in Equation (4) is zero. Once dislocations are generated, U is no longer zero and its value can be determined from the pure bending condition, i.e. from the condition that the net force in the x_1 direction, F_1, defined as:

$$F_1(x_1 = \pm L/2) = \pm \int_{-h/2}^{h/2} \sigma_{11}(\pm L/2, x_2)\, dx_2 = 0 \tag{7}$$

vanishes. Since each stress component can be decomposed into its $\hat{(\ )}$ and $\tilde{(\ )}$ parts, Equation 7 can be rewritten as:

$$F_1(x_1 = \pm L/2) = \pm\left(\int_{-h/2}^{h/2} \hat{\sigma}_{11}(\pm L/2, x_2)\, dx_2 + \int_{-h/2}^{h/2} \tilde{\sigma}_{11}(\pm L/2, x_2)\, dx_2 \right) \tag{8}$$

The second term on the right-hand side of Equation 8 is readily evaluated by superposition using the known positions of dislocations and stress fields for individual dislocations within an isotropic, linear-elastic infinite-medium. The first term on the right-hand side of Equation 8 is evaluated by first determining the $\hat{(\ )}^{(1)}$ fields which are consistent with the following boundary conditions:

$$\hat{\sigma}_{11}^{(1)} = -\tilde{\sigma}_{11}, \quad \hat{\sigma}_{12}^{(1)} = -\tilde{\sigma}_{12} \quad \text{on} \quad x_2 = \pm h/2; \tag{9}$$

$$\hat{u}_1^{(1)} = -\tilde{u}_1 \pm \theta x_2, \quad \hat{\sigma}_{12}^{(1)} = -\tilde{\sigma}_{12}, \quad \text{on} \quad x_1 = \pm L/2. \tag{10}$$

Clearly, the $\hat{(\ )}^{(1)}$ fields account for the effect of dislocation-based boundary tractions and displacements on the prescribed rotation. However, this field does not ensure pure bending i.e. if $\tilde{\sigma}_{11}^{(1)}$ is substituted for $\tilde{\sigma}_{11}$ in Equation 8, a non-zero value of F_1 is generally obtained. To reduce the magnitude of F_1 to zero, a

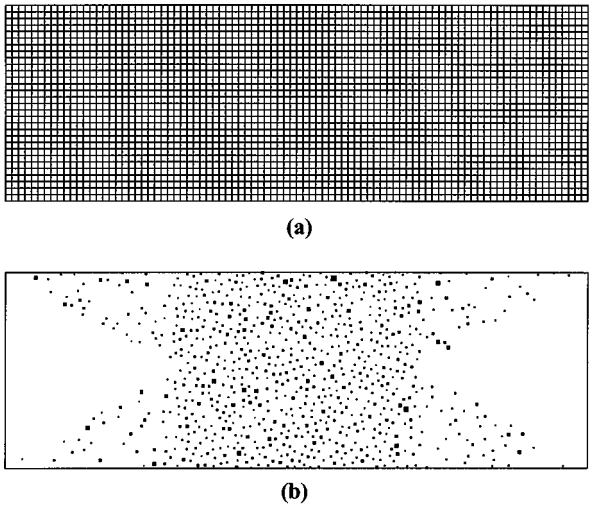

Figure 2 (a) The 90×30 quadrilateral finite-element mesh and (b) the distribution of two-dimensional Frank-Read type dislocation sources used in the present work. Variable size of the symbols is used in (b) to denote the variation in the strength of the sources. The smaller the source strength, the larger the symbol.

uniform uniaxial stress field:

$$\hat{\sigma}_{11}^{(2)} = -\frac{F_1(x_1 = L/2)}{h} \tag{11}$$

needs to be applied. It can be readily shown that the quantity U appearing in Equation 4 is related to $\hat{\sigma}_{11}^{(2)}$ as:

$$U = -\frac{\hat{\sigma}_{11}^{(2)}(1-\nu)L}{2\mu} \tag{12}$$

The displacement U is calculated separately for $x_1 = L/2$ and $x_1 = -L/2$. Since both $\hat{\sigma}^{(1)}$ and $\tilde{\sigma}^i$ stress fields are self-equilibrating, the two U values should be identical. Numerical evaluation of U is found to be quite accurate causing the two U values to differ only at the fourth significant digit. It should be noted that the quantity U is not used in the calculation of the complementary ($\hat{}$) fields but rather these fields are obtained as the superposition of the $(\hat{})^{(1)}$ and the $(\hat{})^{(2)}$ fields.

A beam having dimensions $L = 1.2\,\mu$m and $h = 4\,\mu$m subjected to a bending rate of $\dot{\theta} = 0.5 \times 10^3\ \text{s}^{-1}$ is used in all calculations. The computational domain is discretized into 90×30 isoparametric plane-strain quadrilateral elements, Fig. 2a. Contour plots for the σ_{11} stress (the results not shown for brevity) indicate that the finite element formulation used can reproduce the bending stress distribution in the elastic regime with only minor end effects (<0.2% of σ_{11}). Also, the corresponding bending moment is found to be within 0.2% of its exact value $M = \frac{Eh^3}{12(1-\nu^2)}(\frac{2\theta}{L})$.

In all calculations, three slip systems are considered: two of them are oriented at $\varphi = \pm 30^\circ$ from the x_1-axis while the third one is parallel to the x_2-axis ($\varphi = +90^\circ$). In order to avoid numerical difficulties which may arise when dislocations try to exit the beam through the sides, along which the displacements are prescribed, only the $\pm 30^\circ$ slip planes which do not intersect the sides are considered. The 90° slip planes are introduced only over the central zone of width $L - h/\tan 30^\circ$ within which the $\pm 30^\circ$ slip planes intersect. The slip plane spacing is set to 100 Burgers vectors (25 nm) resulting in a total of 404 slip planes. The material is taken to be initially dislocation-free and to contain, 808 dislocation sources (two per slip plane), Fig. 2(b). The results pertaining to the bending, moment M which will be presented and discussed in Section 3 are all normalized relative to a reference moment, M_{ref} defined as:

$$M_{\text{ref}} = \frac{2}{h}\int_{-h/2}^{h/2} \bar{\tau}_{\text{nuc}} x_2^2\, dx_2 = \frac{2}{3}\bar{\tau}_{nuc}\left(\frac{h}{2}\right)^2 \tag{13}$$

which corresponds to the linear distribution of the σ_{11} stress: $\sigma_{11} = \bar{\tau}_{\text{nuc}} x_2/(h/2)$, in the through-the-height direction.

2.2. Crystal-plasticity formulation

In this section, a plane-strain bending analysis of the beam shown in Fig. 1 is carried out using a continuum crystal-plasticity material constitutive formulation. In order to facilitate a direct comparison with the discrete-dislocation based results, a small displacement-gradient version of this formulation is used [9]. Within this formulation, the total strain rate $\dot{\varepsilon}$ can be written as:

$$\dot{\varepsilon} = \dot{\varepsilon}^e + \dot{\varepsilon}^p \tag{14}$$

where the elastic strain rate $\dot{\varepsilon}^e$ is given in terms of the stress rate $\dot{\sigma}$ by the generalized Hooke's law:

$$\dot{\varepsilon}^e = C^{-1}[\sigma] \tag{15}$$

and the plastic strain rate $\dot{\varepsilon}^p$ is given by:

$$\dot{\varepsilon}^p = \sum_\alpha \dot{\gamma}^\alpha P^\alpha \quad \alpha = 1, 2, 3 \tag{16}$$

C in Equation (15) is a forth-order isotropic elasticity tensor defined as:

$$C = \frac{E}{1+\nu}\left[I' + \frac{\nu}{1+\nu} I \otimes I\right] \tag{17}$$

where I and I' are the second- and the forth-order identity tensors, respectively, and $\otimes$ denotes a tensorial product. $\dot{\gamma}^\alpha$ in Equation 16 represents the shear rate on slip system α characterized by a unit plane normal n^α and a unit slip direction m^α. P^α in Equation 16 is a second-order symmetric Schmid tensor associated with the slip system α and is defined as:

$$P^\alpha = \frac{1}{2}[m^\alpha \otimes n^\alpha + n^\alpha \otimes m^\alpha] \tag{18}$$

In accordance with the discrete-dislocation formulation presented in the previous section three slip systems ($\alpha = 1, 2, 3$) are considered, two inclined at $\pm 30^\circ$ with respect to the x_1' axis and the third one normal to it. Inverting Equation 15 and combining the resulting equation with Equations 14 and 16 yields:

$$\dot{\sigma} = C\left[\dot{\varepsilon} - \sum_\alpha \dot{\gamma}^\alpha P^\alpha\right] \tag{19}$$

Since the discrete-dislocation formulation discussed in the previous section is rate dependent due to the

assumed dislocation velocity law, Equation 2, the continuum material treated in the present section is taken to be viscoplastic. Furthermore, it is assumed that the shear rate on either of the three slip systems is given by the following power-law relation:

$$\dot{\gamma}^{\alpha} = \dot{\gamma}_0 \left[\frac{\tau^{\alpha}}{s^{\alpha}} \right]^{1/m} \quad \text{sign}(\tau_{\alpha}) \tag{20}$$

where $\dot{\gamma}_0$ is a reference shear strain rate, m, the strain-rate sensitivity parameter, τ^{α}, the resolved shear stress and s^{α}, the slip resistance all associated with slip system α. In all calculations $\dot{\gamma}_0 = 0.001$ and $m = 0.005$ were used. As will be discussed later, a low value for $m(<0.01)$ is needed to promote shear band formation at small strains.

In general, the magnitude of slip resistance s^{α} increases during deformation as a result of self-hardening and latent-hardening phenomena. Consequently, an evolution equation for s^{α} has to be defined. In the present work, however, neither self-hardening nor latent-hardening effects are explicitly considered and, hence, an evolution equation for s^{α} is not needed. Instead, in order to mimic the distributions of strengths of the dislocation sources, the places where slip originates within the discrete-dislocation framework, a corresponding distribution of initial slip resistance is used. This approach should enable for slip to be initiated and controlled by the elements with the most favorable combination of a low slip resistance and a high resolved shear stress, the same elements which contain dislocation sources with an optimum combination of a low source strength and a high Peach-Koehler force. As will be shown later, this approach promotes localization of (continuum) plastic flow into narrow bands, which resemble the slip bands which characterize the plastic flow within the discrete-dislocation approach. Furthermore, the resistance to the extension of such bands exerted by the surrounding elements with a higher slip resistance and by other (intersecting) bands implicitly account for self hardening and latent hardening, respectively.

The resolved shear stress on slip system α, τ^{α}, is defined as:

$$\tau^{\alpha} = \sigma \cdot P^{\alpha} \tag{21}$$

where the raised dot is used to denote a scalar product. Substitution of Equations 20 and 21 into Equation 19 yields a stress evolution equation in the form:

$$\dot{\sigma} \, f(\sigma) \tag{22}$$

Euler forward integration scheme is used to integrate this equation so that the stress rate at the end of a time step (time $= t + \Delta t$), $\dot{\sigma}_{t+\Delta t}$ is evaluated using the stress at the beginning of the time increment, σ_t. This integration procedure is incorporated into Vectorized User Material Subroutine (VUMAT) of the commercial finite element program Abaqus/Explicit [10]. To make the calculations more efficient, the materials density is increased by two orders of magnitude. Such density-scaled procedure did not affect the quasi-static results considerably since the kinetic energy never increased above 0.1% of the total energy of deformation.

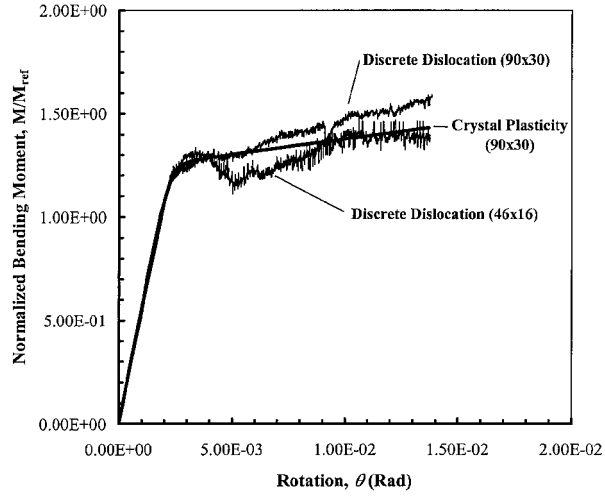

Figure 3 Normalized bending moment M/M_{ref} vs. rotation angle θ relationship predicted by the discrete-dislocation and the crystal-plasticity analyses.

3. Results

3.1. Discrete-dislocation formulations

Fig. 3 shows the variation of the normalized bending moment M/M_{ref} with the angle of rotation θ. Before the onset of dislocation nucleation, beam bending is purely elastic and, thus, a linear relationship exists between M/M_{ref} and θ. When the normalized bending moment reaches a value of $\sim$1.21 the first dislocation dipole nucleates and beyond this point the M/M_{ref} vs. θ relationship is no longer linear. Nevertheless M/M_{ref} continues to increase with θ but at a lesser rate until it reaches a local maximum value of $\sim$1.33. Subsequently, M/M_{ref} decreases to a local minimum ($\sim$1.27) and then begins to increase again at a nearly constant rate. The M/M_{ref} vs. θ relationship in the "plastic" regime is not smooth but rather characterized by high-frequency fluctuations whose occurrence is the consequence of discrete dislocation events (e.g. dipole nucleation or annihilation, dislocations reaching the free surface, etc.). Occasionally, the M/M_{ref} vs. θ curve develops a major spike (e.g. the one at $\theta \approx 0.09$), which indicates a significant rearrangement in the dislocation structure such as the one which occurs when one dislocation pile-up begins to penetrate through another one.

In classical plasticity, plastic yielding is assumed to initiate at the free-surfaces of the beam. The bending moment at the onset of plastic yielding M_{y} is then related to the material's yield stress σ_{y} through $M_{\text{y}} = 2\sigma_y(h/2)^2/3$. Using this relationship and $M_{\text{y}}/M = 1.21$, the yield stress is evaluated as $\alpha_y \approx 60.5$ MPa. However, it should be noted that within the discrete-dislocation framework, this value of the yield stress should be considered unique to bending and to a given distribution of dislocation sources.

To demonstrate the effect of loading type on the magnitude of yield stress, the same beam used in the bending analysis, Fig. 1, with the same distribution of sources, is subjected to plane strain tension, with the loading applied in the x_1-direction. The boundary conditions used

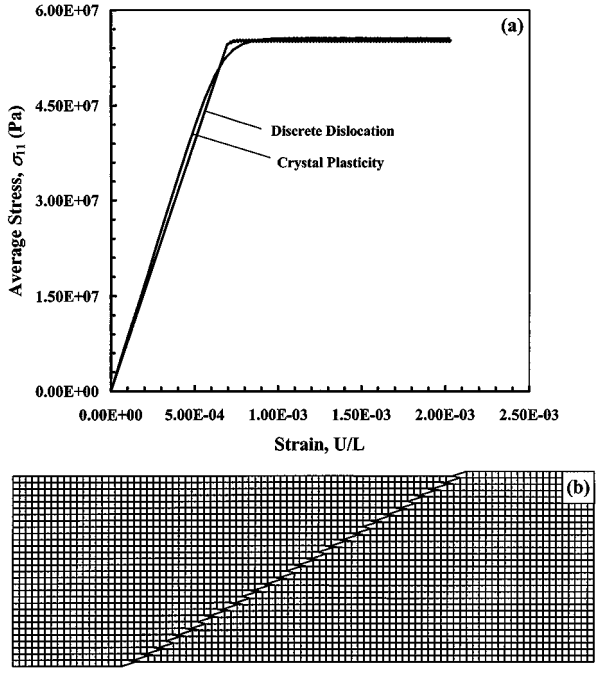

Figure 4 Plane strain tension results of: (a) Axial stress vs. axial strain from discrete-dislocation and crystal-plasticity analyses and (b) the deformed finite element mesh, at the axial strain $\varepsilon = 0.002$ obtained in the discrete-dislocation analysis.

in this case include stress-free surfaces at $x_2 = \pm h/2$ and a uniform distribution of tensile x_1 displacements and the zero shear stress condition along the beam sides at $x_1 = \pm L/2$. The axial stress vs. axial strain results obtained, Fig. 4a, indicate that the deviation from the linear elastic behavior first occurs at the stress level $\sigma = 55$ MPa, which is approximately 10% smaller than the yield stress value ($\sigma_y = 60.5$ MPa) deduced in the bending analysis. This difference can be readily explained. In the case of plane-strain tension, the stress is uniform throughout the beam, hence, the magnitude of the yield stress is solely controlled by the dislocation source associated with the lowest strength. In the case of bending, on the other hand, the stress field is non-uniform and hence the yield stress is controlled by both the source strength and by the magnitude of the slip-plane resolved shear stress acting on the source. Consequently, initial yielding is not generally associated with the source of minimum strength. The deformed mesh corresponding to the axial (plane-strain tension) stran $\varepsilon = 0.002$ is shown in Fig. 4b. The mesh clearly shows that plastic flow has localized on one slip plane, which, as demonstrated by the results shown in Fig. 4a, gives rise to a plateau in the stress-strain curve. The dislocation structure (the results not shown for brevity) reveals a very low density of well separated dislocations gliding on a single slip plane. The dislocation density does not change substantially during deformation. This dislocation structure is consistent with the fact that due to the localization of the slip on one plane, forest-dislocation type obstacles do not form and the dislocations are free to exit the beam through the free surfaces at $x_2 = \pm h/2$. In addition, this finding is consistent with the observed plateau in the stress-strain curve.

The mesh dependence of the normalized moment vs. rotation angle curve is shown in Fig. 3 where the results for a coarser 46×16 mesh are presented in addition to the ones for the 90×30 mesh. The values of the bending moment at the onset of plastic yielding are quite comparable in the two cases. However, the peak values and the local minimum values differ considerably. The rates of strain hardening in the later stages of plastic deformation are quite similar in the two cases but the level of the normalized bending moment is lower in the case of the coarser mesh by about 0.12. The observed effect of the mesh size could be the result of one or more of the following factors: (a) potential differences in the resolution of the $\hat{(\ )}$ fields; (b) differences in discretization of the nodal values of $\tilde{\sigma}_{ij}$ stress components which are used to construct the loading term for the $\hat{(\ )}$ fields; (c) differences in the accuracy of numerical integration of the stress field along $x_1 = \pm L/2$ beam sides.

The dislocation structure at three values of the rotation angle θ are shown in Fig. 5a–c. Dislocation pile-ups consisting of positive dislocations on the slip planes inclined at $+30^\circ$ relative to the positive x_1-axis and of negative dislocations on slip planes inclined at -30° relative to the positive x_1-axis can be seen at each level of the rotation angle. Since dislocations are nucleated as dipoles and only dislocations of one sign are observed on any given plane, this implies that the missing dislocations have exited the beam through the top or bottom free surfaces. The remaining dislocations give rise to plastic bending and can be considered as "geometrically necessary" in order to account for the gradient in plastic strain along the slip planes. However, not all the dislocations seen in Fig. 5a–c are geometrically necessary. For example, a few dislocations are observed on the $\phi = +90^\circ$ slip planes. These dislocations do not contribute to plastic bending and hence, are not geometrically necessary. The density of such "statistical" dislocations is small at low values of the rotation angle (e.g. $\theta = 0.005$, Fig. 5a). At this stage the M/M_{ref} vs. θ curve in Fig. 3 is rather flat. The interactions of both geometrically necessary and statistical dislocations on intersecting slip systems, Fig. 5b and c, creates barriers to dislocation motion, which gives rise to the observed strain hardening, Fig. 3.

The deformed meshes at the same three values of the rotation angle as in Fig. 5a–c are shown in Fig. 6a–c. The slip steps which can be seen on the free surfaces of the beam are caused by the dislocations which have exited the beam. As discussed earlier, the highly localized deformation pattern, seen in Fig. 6a–c is a consequence of the localized nature of displacement fields of the individual dislocations and of the concentration of dislocation activity on only few slip planes. Hence, the localization of the deformation fields observed should not be considered as an indication of a mesh dependent solution typically observed in the analysis of rate-independent elastic-plastic materials, but rather an indication of highly localized displacement fields of the dislocation pile-ups. As will be shown below, the wavelengths of the $\hat{(\ )}$ fields are large relative to the characteristic mesh length and, hence, the observed localization of deformation can not be related to the one observed in rate-independent analyses.

Contour plots of the σ_{11} stress at the same three values of the rotation angle are shown in Fig. 7a–c. As

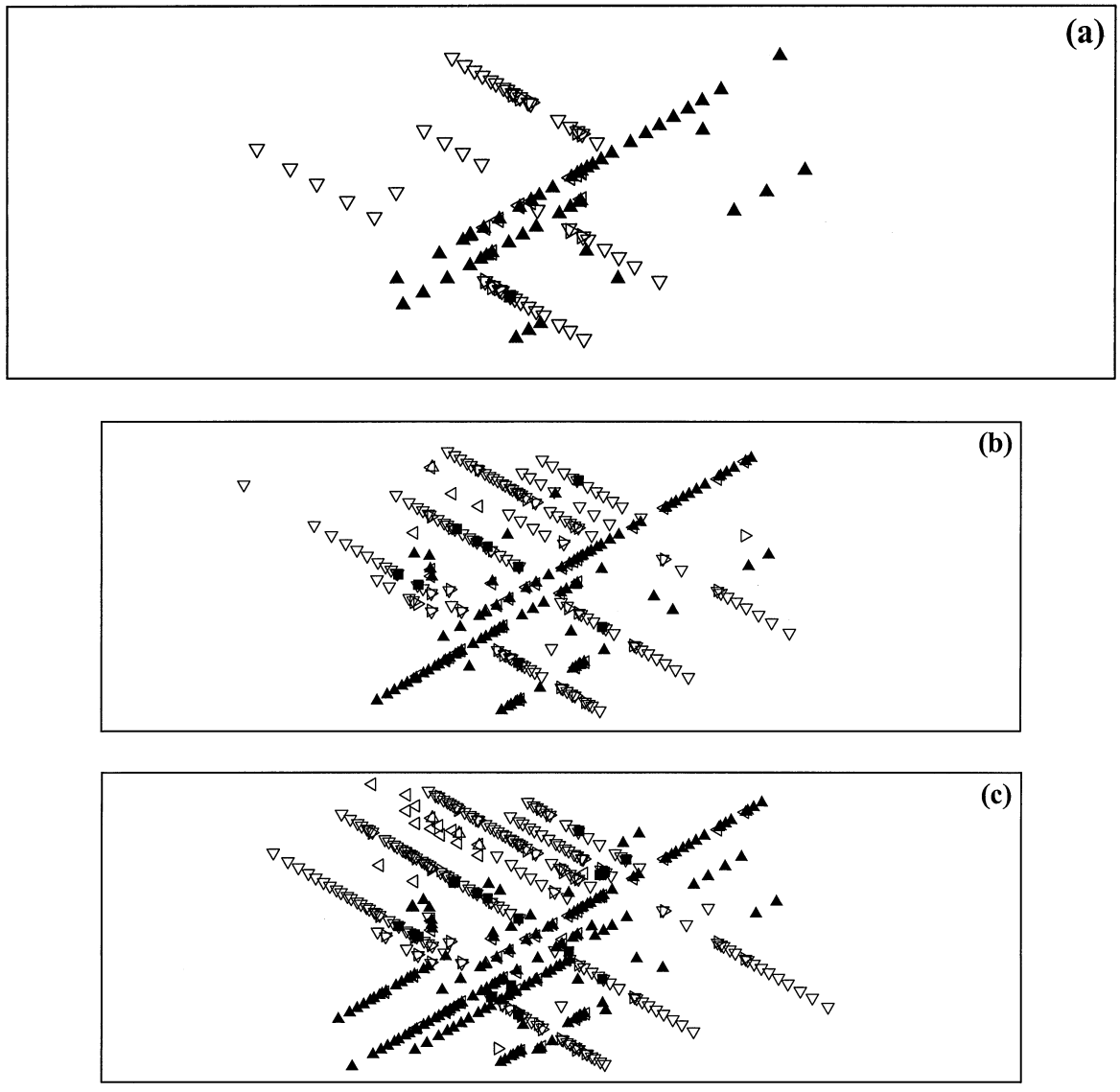

Figure 5 The distribution of dislocations at three values of the rotation angle: (a) $\theta = 0.005$; (b) $\theta = 0.010$ and (c) $\theta = 0.015$. ▲, △ and ▷ are used to denote positive and ▼, ▽ and ◁ negative dislocations on the $\phi = +30^\circ, -30^\circ$, and 90°, respectively.

expected, the σ_{11} stress is tensile in the upper and compressive in the lower portion of the beam. However, the σ_{11} stress field is not very smooth in the middle region of the beam, which is the result of the effect of a high local density of dislocations. A contour plot of the complementary $\hat{\sigma}_{11}$ stress field at the rotation angle $\theta = 0.010$ is shown in Fig. 8a. The complementary stress is also tensile in the upper and compressive in the lower portion of the beam. However, relative to the σ_{11} stress field, this field is very smooth. A contour plot of the corresponding discrete-dislocation based $\tilde{\sigma}_{11}$ stress at the same value of $\theta = 0.01$ is shown in Fig. 8b. Since the stress fields of individual dislocations are singular and decay inversely with distance from the dislocation, their effect is visible where the dislocations are very close to the nodal points. As evident from Fig. 8b, the collective dislocation structure gives rise to a high tensile σ_{11} stress in the lower and to a high compressive stress in the upper region of the beam. Since the discrete-dislocation $\tilde{\sigma}_{11}$ stress fields and the complementary $\hat{\sigma}_{11}$ stress fields are of opposite sign over much of the beam, the magnitude of the corresponding total $\sigma_{11} = \hat{\sigma}_{11} + \tilde{\sigma}_{11}$ stress is considerably reduced.

As discussed earlier, dislocations generated on the $\phi = \pm 30^\circ$ slip system are geometrically necessary. The density of geometrically necessary dislocations is a function of the plastic rotation angle, θ^p, defined by Ney [2] and Ashby [3] as:

$$\rho_G = \frac{n_G}{Lh} = \frac{\theta^p}{Lb_1} \tag{23}$$

where n_G is the number of geometrically necessary dislocations, b_1 the component of the Burgers vector parallel to the x_1-axis and is given as: $b_1 = b\cos\phi$. θ^p can be defined as $\theta^p = \theta - \theta^e$ where θ^e is the elastic rotation angle, which is related to the bending moment as:

$$M = \frac{Eh^3}{12(1-\nu^2)}\left(\frac{2\theta^e}{L}\right). \tag{24}$$

At each level of the total rotation angle θ, θ^e can be determined by inverting Equation 24 and using the value of the corresponding bending moment as given in Fig. 3. Then θ^p can be determined from $\theta^p = \theta - \theta^e$ and the

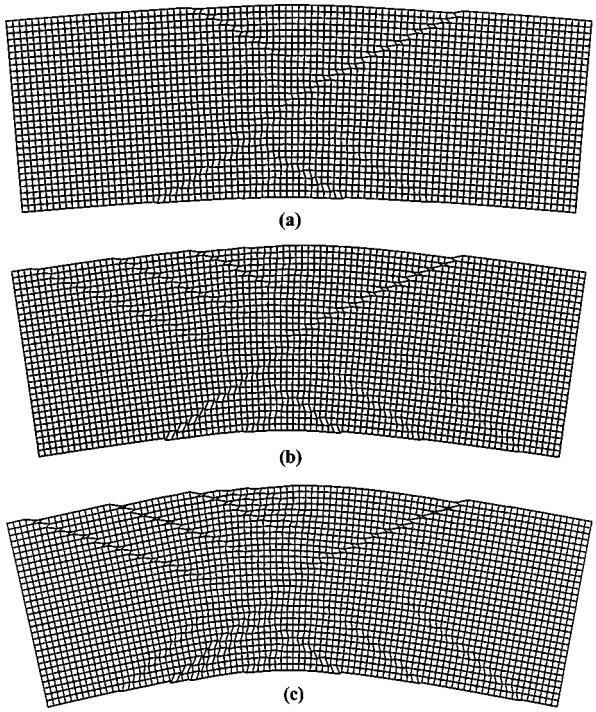

Figure 6 Deformed finite element meshes obtained in the discrete-dislocation analysis of plane strain beam bending at the three values of the rotation angle indicated in Fig. 5.

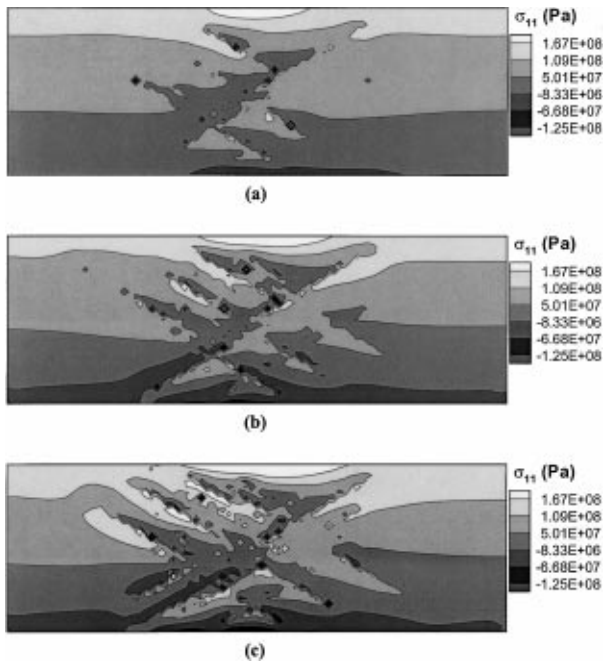

Figure 7 Contour plots of the σ_{11} stress obtained in the discrete-dislocation analysis of plane-strain beam bending at the three values of the rotation angle indicated in Fig. 5.

predicted number of geometrically necessary dislocations, n_G, computed from Equation 23. This number can then be compared to the number of dislocations observed in the corresponding dislocation structure, Fig. 5a–c.

Following the procedure outlined above it is found that: (a) the observed number of dislocations is generally 20–30% higher than the predicted one. This indicates that a significant fraction of dislocations are statistically stored rather than geometrically necessary; and,

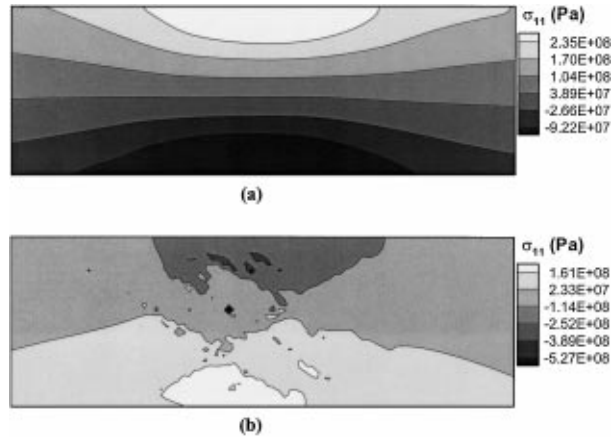

Figure 8 Contour plots of: (a) the $\hat{\sigma}_{11}$ stress and; (b) the $\tilde{\sigma}_{11}$ stress obtained in the discrete-dislocation analysis of plane-strain beam bending at the rotation angle $\theta = 0.010$. The corresponding contour plot for the total stress $\sigma_{11} = \tilde{\sigma}_{11} + \hat{\sigma}_{11}$ is shown in Fig. 7b.

(b) a nearly linear increase in the dislocation density with the plastic rotation angle, which is in accordance with Equation 23. The slope of the ρ_G vs. θ^P line (the results not shown for brevity) is found to be within 10% of the value $1/Lb_1$ predicted by Equation 23.

3.2. Crystal-plasticity formulation

The discrete-dislocation modeling results presented and discussed in the previous section, clearly established that one of the salient features of the plastic flow behavior at the micron-length scale is its localization into slip bands. Hence, a continuum-plasticity model which may be proposed to replace the discrete-dislocation analysis must be able to reproduce this feature of plastic deformation at the micron-length scale. In a series of papers by Asaro and co-workers [e.g. 11, 12], it was shown that the crystal-plasticity model of the type used in the present work can give rise to the localization of plastic flow into shear bands. However, such localization takes place only after at least a few percent of "uniform" plastic strain. Localization of the plastic flow into slip bands observed in the discrete-dislocation analysis, Fig. 6a, on the other hand, takes place from the very onset of plastic deformation. To promote plastic-flow localization at small strains within the crystal-plasticity model used in the present work, the strain rate sensitivity parameter m is set to a low value ($m = 0.005$) and the initial deformation resistance of an element is assumed to be proportional to the strength of the dislocation source(s) it contains. This procedure ensures that the plastic flow is initiated in the elements containing the most active dislocation sources.

Localization of the plastic flow in shear bands is accompanied by a significant rotation of the crystal lattice. However, slip bands resulting from dislocation glide, preserve the orientation of the crystal lattice. To resolve this discrepancy, a small displacement-gradient formulation of the crystal plasticity theory discussed in Section 2.2 is used which does not provide for lattice rotation.

Contour plots of the equivalent plastic strain at three levels of the total axial strain obtained in the crystal-plasticity analysis of the beam in plane-strain tension,

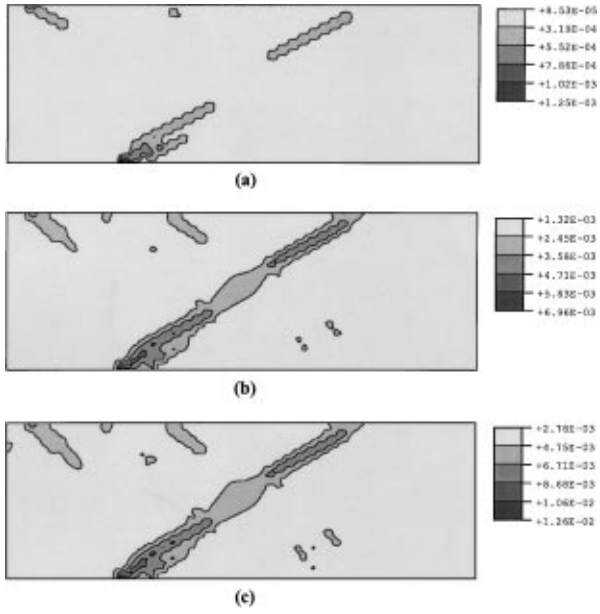

Figure 9 Contour plots of the equivalent plastic strain obtained in the crystal-plasticity analysis of plane-strain tension at three values of the axial strain: (a) 0.001, (b) 0.002, and (c) 0.003.

are shown in Fig. 9a–c. Distorted finite element meshes are not shown since, in this case, localization of the plastic flow in deformation bands is not as well developed as in the discrete-dislocation analysis and is more difficult to infer from the distorted meshes. The results shown in Fig. 9a–c, indicate that during plane-strain tension plastic flow mainly localizes into a band whose location coincides with the slip band observed in Fig. 4b. As the imposed axial strain increases, localization of the plastic flow becomes more pronounced.

As discussed earlier, the initial slip resistance of each element is assumed to be proportional to the value of the dislocation-source strength τ_{nuc} it contains. The initial slip resistances of the elements which do not contain dislocation sources is set to scale with $1.2\ \bar{\tau}_{\text{nuc}}$, which is one standard deviation higher than $\bar{\tau}_{\text{nuc}}$. The slip-resistance/source-strength proportionality constant is determined by fitting the axial-stress vs. axial strain plane-strain tension curve obtained using the discrete-dislocation approach, Fig. 4a. The result of the fitting procedure is also shown in Fig. 4a. It is evident that the discrete-dislocation based results for plane-strain tension can be reproduced fairly well by the continuum crystal-plasticity model, at least in the small strain range analyzed in the present work. The advantage of the crystal-plasticity analysis is that it could be completed in only a fraction (typically 1–2%) of the time required for completion of the corresponding discrete-dislocation analysis. It should be noted, however, that in our discrete-dislocation analysis a Fortran-based computer program is interfaced with the commercial finite element program Abaqus/Standard [10] which requires linking of the two at each time step. Consequently, more modest reductions in computer time are to be expected should the discrete-dislocation analysis be carried out using a single computer program.

The variation of the normalized bending moment M/M_{ref} with the angle of rotation θ as predicted by the crystal plasticity analysis is shown in Fig. 3. A comparison of the discrete-dislocation plasticity and crystal-plasticity based results shown in Fig. 3 indicate that: (a) while yielding takes place at any non-zero level of the applied stress within the crystal-plasticity framework, a visible deviation of the M/M_{ref} vs. θ curve from linear elastic behavior occurs at a value of M/M_{ref} which is quite comparable to that predicted by the discrete-dislocation analysis; (b) in spite of the fact that no explicit account of strain hardening of the material is taken into account, the M/M_{ref} vs. θ curve increases in the plastic region. This observation can be attributed to the effect of intersecting deformation bands which impede each others propagation and due to the extension of the shear bands into the surrounding material with a higher slip resistance; and (c) the rate of strain hardening predicted by the crystal-plasticity analysis is substantially smaller than that predicted by the discrete-dislocation plasticity. This implies that the interaction of the deformation bands is not strong enough in comparison to the long- and short-range interactions between discrete dislocations and hence can not fully account for the hardening effects observed within the discrete-dislocation plasticity analysis. In addition, conventional crystal plasticity does not account for additional hardening which arises from the presence of geometrically necessary dislocations.

A contour plot of the equivalent plastic strain at the rotation angle $\theta = 0.010$ is shown in Fig. 10a. Localization of plastic deformation into broad deformation bands and intersections of these bands are evident. A comparison of the results shown in Fig. 10a with the ones shown in Fig. 6b shows that there is a crystallographic relationship between the deformation bands predicted by the crystal-plasticity analysis and the slip bands obtained in the discrete-dislocation analysis. Thus one of the salient features of plastic deformation at the micron-length scale, the localization of plastic flow, is predicted in the crystal plasticity analysis of beam bending.

A contour plot of the σ_{11} stress at the rotation angle $\theta = 0.010$ is shown in Fig. 10b. Since the plastic flow localization if controlled by the elements with a low slip resistance and strain hardening is not considered explicitly, there is a close relationship between the

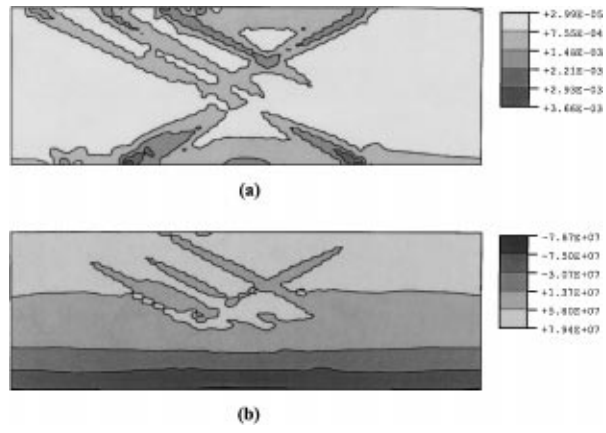

Figure 10 Contour plots of: (a) the equivalent plastic strain; and (b) the σ_{11} stress obtained in the crystal-plasticity analysis of plane-strain bending at the rotation angle: (a) $\theta = 0.010$. The discrete-dislocation plasticity contour plot corresponding to (b) is shown in Fig. 7b.

equivalent plastic strain contour plot, Fig. 10a, and the σ_{11} stress contour plot, Fig. 10b. A comparison of the results shown in Fig. 10b with the ones shown in Fig. 7b shows that: (a) The maximum stress levels predicted by the crystal-plasticity analysis, Fig. 10b, are considerably smaller than the corresponding ones predicted by the discrete-dislocation plasticity analysis, Fig. 7b. This observation is consistent with the lower rate of strain hardening predicted by the crystal-plasticity approach, Fig. 3. Generation of dislocation pile-ups which act as load springs is the principle cause of high stresses obtained within the discrete-dislocation analysis. As stated earlier, the interactions of deformation bands within the crystal-plasticity approach are too weak to give rise to a significant increase in the bending moment in the plastic region; and (b) In addition to failing to predict the correct maximum stress levels, the crystal-plasticity analysis is not able to reveal many details in the stress fields observed within the discrete-dislocation analysis, Fig. 7b. This limitation of the crystal-plasticity approach could be critical if the present analysis is to be extended to include initiation of failure which may be controlled by local buildup in stress.

Some of the deficiencies of the crystal-plasticity model used can be overcome if non-local effects are to be included. Within a non-local crystal-plasticity formulation, the constitutive behavior of the material depends both on strain and strain gradient. The relationship between plastic strain gradient and geometrically necessary dislocations is well-established [e.g. 13]. Thus, as bending proceeds and, as discussed in the previous section, the density of geometrically necessary dislocations increases, the plastic strain gradient also increases, giving rise to a higher deformation resistance. This, in turn, would result in a larger rate of strain hardening in the M/M_{ref} vs. θ relationship, Fig. 3. In addition, localized regions with high stresses of the type predicted by the discrete-dislocation analysis are more likely to develop. A non-local crystal-plasticity model for the analysis of deformation behavior of the material at the micron-length scale is currently being developed [14].

4. Discussion

5. Conclusions

The main objective for the present work was to analyze plane-strain bending of a micron-size beam using both a discrete-dislocation plasticity formulation and a continuum crystal-plasticity formulation in order to determine if a computationally less costly continuum analysis can reproduce the essential feature of the plastic flow associated with the collective motion of discrete dislocations. Since one of the salient features of the discrete-dislocation plastic flow is its localization into slip bands, material parameters for the continuum crystal-plasticity model are selected in such a way that plastic flow localization into deformation bands occurs even at very small strains. The results obtained suggest that:

(1) Global response of the material at the micron-length scale (e.g. the bending moment vs. rotation angle relationship) can be fairly well reproduced using the continuum formulation;

(2) Plastic flow localizes into deformation bands which are crystallographically related to the discrete-dislocation based slip bands. However, the deformation bands are broader and fewer in number than the corresponding slip bands;

(3) Stress and deformation fields predicted by the continuum model do not generally contain many details of the corresponding discrete-dislocation fields. This discrepancy could be critical when one considers issues such as the onset of damage in the material during deformation which is governed by the local maxima in the stress and/or strain fields.

Acknowledgements

The material presented here is based on work supported by the National Science Foundation, Grant Numbers DMR-9906268 and CMS-9531930 and by the U.S. Army Grant Number DAAH04-96-1-0197. The authors are indebted to Drs. Bruce A. MacDonald and Daniel C. Davis of NSF and Dr. David M. Stepp of ARO for the continuing interest in the present work. The help of Dr. Erik Van der Giessen in providing the preprints of his work and in clarifying some aspects of the computational procedure is greatly appreciated. The authors also acknowledge the support of the Office of High Performance Computing Facilities at Clemson University.

References

1. H. H. M. CLEVERINGA, E. VAN DER GIESSEN and A. NEEDLEMAN, *International Journal of Plasticity* **15** (1999) 837.
2. J. F. NYE, *Acta Metall.* (1953) 153.
3. M. F. ASHBY, *Phil. Mag.* **21** (1970) 399.
4. A. NEEDLEMAN and E. VAN DER GIESSEN, *Model. Simul. Mater. Sci. Eng.* **3** (1995) 689.
5. A. NEEDLEMAN, E. VAN DER GIESSEN and H. H. M. CLEVERINGA, "Comparison of Discrete Dislocation and Continuum Plasticity Predictions for a Composite Material," *Acta Mat.* **45** (1997) 3163.
6. F. R. N. NABARRO, "Theory of Crystal Dislocations" (Oxford University Press, Oxford, 1967).
7. J. LOTHE and J. P. HIRTH, "Theory of Dislocations" (McGraw Hill, New York, 1968).
8. L. P. KUBIN, G. CANOVA, M. CONDAT, E. DEVINCERE, V. PENTOKIS and Y. BRECHET, in "Nonlinear Phenomena in Materials Science II," edited by G. MARTIN and L. P. KUBIN (Sci-Tech, Vaduz, 1992) p. 455.
9. E. VAN DER GIESSEN, A. NEEDLEMAN, "Discrete Dislocation Plasticity: A Simple Planar Model," *Modeling Simul. Mater. Sci. Eng.* **3** (1995) 689.
10. Abaqus Theory Manual, Version 5.8 (Habbit, Karlson and Sorenson, Inc., Providence, RI, 1999).
11. D. PEIRCE, R. ASARO and A. NEEDLEMAN, "Material Rate Dependence and Localized Deformation in Crystalline Solids," *Acta Metall.* **31** (1983) 1951.
12. *Idem.*, "An Analysis of Nonuniform and Localized Deformation in Ductile Single Crystals," *Acta Metall.* **30** (1982) 1087.
13. N. A. FLECK and J. W. HUTCHINSON, "Strain Gradient Plasticity," *Adv. Appl. Mech.* **33** (1997) 295.
14. D. COLUMBUS, MS Thesis Clemson University (in progress).

Received 15 June
and accepted 27 October 2000